

Article

Ratiometric pH Imaging with a Co MRI Probe via CEST Effects of Opposing pH Dependences

Agnes E. Thorarinsdottir, Kang Du, James H. P. Collins, and T. David Harris

J. Am. Chem. Soc., **Just Accepted Manuscript** • DOI: 10.1021/jacs.7b08574 • Publication Date (Web): 13 Oct 2017

Downloaded from <http://pubs.acs.org> on October 13, 2017

Just Accepted

"Just Accepted" manuscripts have been peer-reviewed and accepted for publication. They are posted online prior to technical editing, formatting for publication and author proofing. The American Chemical Society provides "Just Accepted" as a free service to the research community to expedite the dissemination of scientific material as soon as possible after acceptance. "Just Accepted" manuscripts appear in full in PDF format accompanied by an HTML abstract. "Just Accepted" manuscripts have been fully peer reviewed, but should not be considered the official version of record. They are accessible to all readers and citable by the Digital Object Identifier (DOI®). "Just Accepted" is an optional service offered to authors. Therefore, the "Just Accepted" Web site may not include all articles that will be published in the journal. After a manuscript is technically edited and formatted, it will be removed from the "Just Accepted" Web site and published as an ASAP article. Note that technical editing may introduce minor changes to the manuscript text and/or graphics which could affect content, and all legal disclaimers and ethical guidelines that apply to the journal pertain. ACS cannot be held responsible for errors or consequences arising from the use of information contained in these "Just Accepted" manuscripts.



ACS Publications

Ratiometric pH Imaging with a Co^{II} MRI Probe via CEST Effects of Opposing pH Dependences

Agnes E. Thorarinsdottir,[†] Kang Du,[†] James H. P. Collins,[‡] and T. David Harris^{*,†}

[†]Department of Chemistry, Northwestern University, Evanston, Illinois 60208, USA

[‡]Advanced Magnetic Resonance Imaging and Spectroscopy Facility, University of Florida, Gainesville, Florida 32611, USA

ABSTRACT: We report a Co_2 -based magnetic resonance (MR) probe that enables the ratiometric quantitation and imaging of pH through chemical exchange saturation transfer (CEST). This approach is illustrated in a series of air- and water-stable Co^{II} complexes featuring CEST-active tetra(carboxamide) and/or hydroxyl-substituted bisphosphonate ligands. For the complex bearing both ligands, variable-pH CEST and NMR analyses reveal highly-shifted carboxamide and hydroxyl peaks with intensities that increase and decrease with increasing pH, respectively. The ratios of CEST peak intensities at 104 and 64 ppm are correlated with solution pH in the physiological range 6.5–7.6 to construct a linear calibration curve of $\log(\text{CEST}_{104 \text{ ppm}}/\text{CEST}_{64 \text{ ppm}})$ vs pH, which exhibits a remarkably high pH sensitivity of $0.99(7) \text{ pH unit}^{-1}$ at 37°C . In contrast, the analogous Co^{II} complex with a CEST-inactive bisphosphonate ligand exhibits no such pH response, confirming that the pH sensitivity stems from the integration of amide and hydroxyl CEST effects that show base- and acid-catalyzed proton exchange, respectively. Importantly, the pH calibration curve is independent of the probe concentration, and is identical in aqueous buffer and fetal bovine serum. Furthermore, phantom images reveal analogous linear pH behavior. The Co^{II} probe is stable toward millimolar concentrations of $\text{H}_2\text{PO}_4^-/\text{HPO}_4^{2-}$, CO_3^{2-} , SO_4^{2-} , CH_3COO^- , and Ca^{2+} ions, and more than 50% of melanoma cells remain viable in the presence of millimolar concentrations of the complex. The stability of the probe in physiological environments suggests that it may be suitable for *in vivo* studies. Together, these results highlight the ability of dinuclear transition metal PARACEST probes to provide a concentration-independent measure of pH, and they provide a potential design strategy toward the development of MR probes for ratiometric pH imaging.

INTRODUCTION

Acidic extracellular pH features prominently in a number of pathological conditions, including cancer,¹ ischemia,^{1f,2} inflammation,^{1h,2c} and infection.^{1h} As such, the ability to measure and spatially map tissue pH would provide valuable information regarding the role of acidosis in both the initiation and the progression of diseases.^{1–3} Toward this end, magnetic resonance imaging (MRI) represents an ideal non-invasive modality for probing pH, owing to its ability to deeply penetrate tissue and generate images with high spatiotemporal resolution.⁴ Indeed, a number of MR techniques have been developed to measure pH *in vivo*, and these methods commonly rely on the presence of pH-sensitive exogenous molecular probes. Among these probes, complexes that exhibit the paramagnetic chemical exchange saturation transfer (PARACEST) effect, where exchange of protons on a paramagnetic molecule with those of bulk H_2O upon selective irradiation is exploited to generate contrast,⁵ are particularly well suited, due to large hyperfine shifts of their labile protons and the inherent pH sensitivity of their exchange rates.⁶

The intrinsic concentration dependence of the CEST effect intensity requires that the concentration of a PARACEST probe in the imaged region must be known. A number of strategies have been reported to overcome this limitation, including the development of probes with pH-dependent changes in the frequency⁷ or linewidth⁸ of the CEST peak or in the ratio of CEST intensities from two presaturation fre-

quencies.^{7ac,9} Moreover, the ability of these probes to map extracellular pH in biological environments has been demonstrated.^{7c,8,9cegh}

Despite these promising advances, the development of a single probe that features CEST peaks shifted outside the tissue magnetization transfer window,¹⁰ is highly responsive in the physiological pH range, and displays good stability under physiological conditions remains elusive. Toward this end, transition metal-based PARACEST probes^{7d,9f,11} offer potential advantages over their more common lanthanide counterparts. Specifically, the chemical shifts of transition metal complexes are primarily governed by through-bond interactions rather than the dominant through-space interactions of lanthanide complexes, which renders exchangeable protons extremely sensitive to the metal coordination environment and thus amenable to the design of responsive probes.¹²

In conjunction with the employment of transition metal ions, one can envision incorporation of two distinct ligand scaffolds on a single complex, where the two ligands exhibit CEST effects with opposing pH dependences. For such a system, the ratio of the two CEST peak intensities should change dramatically as a function of pH. Along these lines, we recently reported Fe_2 , Cu_2 , and CuGa complexes supported by a modular dinucleating tetra(carboxamide) ligand and bisphosphonate ancillary ligands.^{11lm} Among these ancillary ligands, etidronate notably features a pendent hydroxyl group that can potentially give rise to CEST. Indeed, the presence of both base-catalyzed exchange of carboxamide protons and

acid-catalyzed proton exchange of etidronate highlights the potential of these dinuclear complexes to exhibit pronounced pH sensitivity. Accordingly, we herein report a Co^{II}_2 complex that displays CEST spectra featuring highly pH-sensitive and shifted peaks, by virtue of CEST-active carboxamide and hydroxyl groups with opposing pH dependences. The complex exhibits excellent chemical stability and retains its CEST activity in fetal bovine serum, which underscores the potential suitability of this and related complexes for pH quantitation in living systems.

EXPERIMENTAL SECTION

General Considerations. Unless otherwise specified, the manipulations described below were carried out at ambient atmosphere and temperature. Air- and water-free manipulations were performed under a dinitrogen atmosphere in a Vacuum Atmospheres Nexus II glovebox or using standard Schlenk line techniques. Glassware was oven-dried at 150 °C for at least 4 h and allowed to cool in an evacuated antechamber prior to use in the glovebox. Acetonitrile (MeCN), diethyl ether (Et_2O), diisopropylethylamine (DIPEA), and methanol (MeOH) were dried using a commercial solvent purification system from Pure Process Technology and stored over 3 or 4 Å molecular sieves prior to use. The solvent H_2O was obtained from a purification system from EMD Millipore. Deuterated solvents were purchased from Cambridge Isotope Laboratories and Sigma Aldrich. The synthesis of 2,2'-iminobis(acetamide) was carried out according to a previously reported procedure.¹¹ Anhydrous hydrogen chloride gas was generated by adding concentrated hydrochloric acid to a stirring solution of concentrated sulfuric acid. The gas was passed through a

bubbler filled with concentrated sulfuric acid. All other reagents and solvents were purchased from commercial vendors and used without further purification. Experimental details on the synthesis of ligands and organic precursors are provided in the Supporting Information.

Synthesis of $\text{Na}[\text{LCo}_2(\text{etidronate})]\cdot 0.2\text{NaNO}_3\cdot 2.7\text{H}_2\text{O}$ (1). A pink solution of $\text{Co}(\text{NO}_3)_2\cdot 6\text{H}_2\text{O}$ (71 mg, 0.24 mmol) in MeOH (2 mL) was added dropwise to a stirring yellow suspension of HL (52 mg, 0.12 mmol) in MeOH (3 mL) to give a dark orange solution. To this solution, a colorless solution of etidronic acid monohydrate (27 mg, 0.12 mmol) in MeOH (2 mL) was added dropwise to give a light orange solution. Subsequent addition of sodium methoxide (33 mg, 0.61 mmol) in MeOH (2 mL) resulted in the formation of a light orange slurry. After stirring at 25 °C for 3 h, the orange solid was collected by vacuum filtration, washed with MeOH (5 mL) and Et_2O (15 mL), and dried under reduced pressure for 16 h to give **1** (44 mg, 44%) as an orange solid. Anal. Calcd. for $\text{C}_{18}\text{H}_{31.4}\text{Co}_2\text{N}_{7.2}\text{Na}_{1.2}\text{O}_{17.3}\text{P}_2$: C, 25.96; H, 3.80; N, 12.11%. Found: C, 25.96; H, 3.83; N, 12.16%. ICP-OES: Co:P = 1.02:1.00. UV-Vis absorption spectrum (64 μM ; 50 mM 4-(2-hydroxyethyl)-1-piperazineethanesulfonic acid (HEPES) buffered at pH 7.4, 25 °C): 375 nm (ϵ = 13800 $\text{M}^{-1}\text{cm}^{-1}$). ESI-MS (m/z): Calcd. for $\text{C}_{18}\text{H}_{26}\text{Co}_2\text{N}_7\text{O}_{14}\text{P}_2$ ($[\text{LCo}_2(\text{etidronate})]^-$): 743.97, found: 743.95; calcd. for $\text{C}_{18}\text{H}_{28}\text{Co}_2\text{N}_7\text{O}_{14}\text{P}_2$ ($[\text{LCo}_2(\text{etidronate})+2\text{H}]^+$): 745.98, found 745.92. FT-IR (ATR, cm^{-1}): 3341 (m, broad); 3178 (m, broad); 2930 (w); 1665 (s); 1595 (m); 1499 (w); 1446 (m); 1307 (s); 1097 (s); 1060 (s); 911 (m); 826 (w); 799 (m); 751 (w); 706 (m); 539 (s); 470 (s). Slow diffusion of MeCN vapor into a concentrated solution of **1** in H_2O afforded dark orange

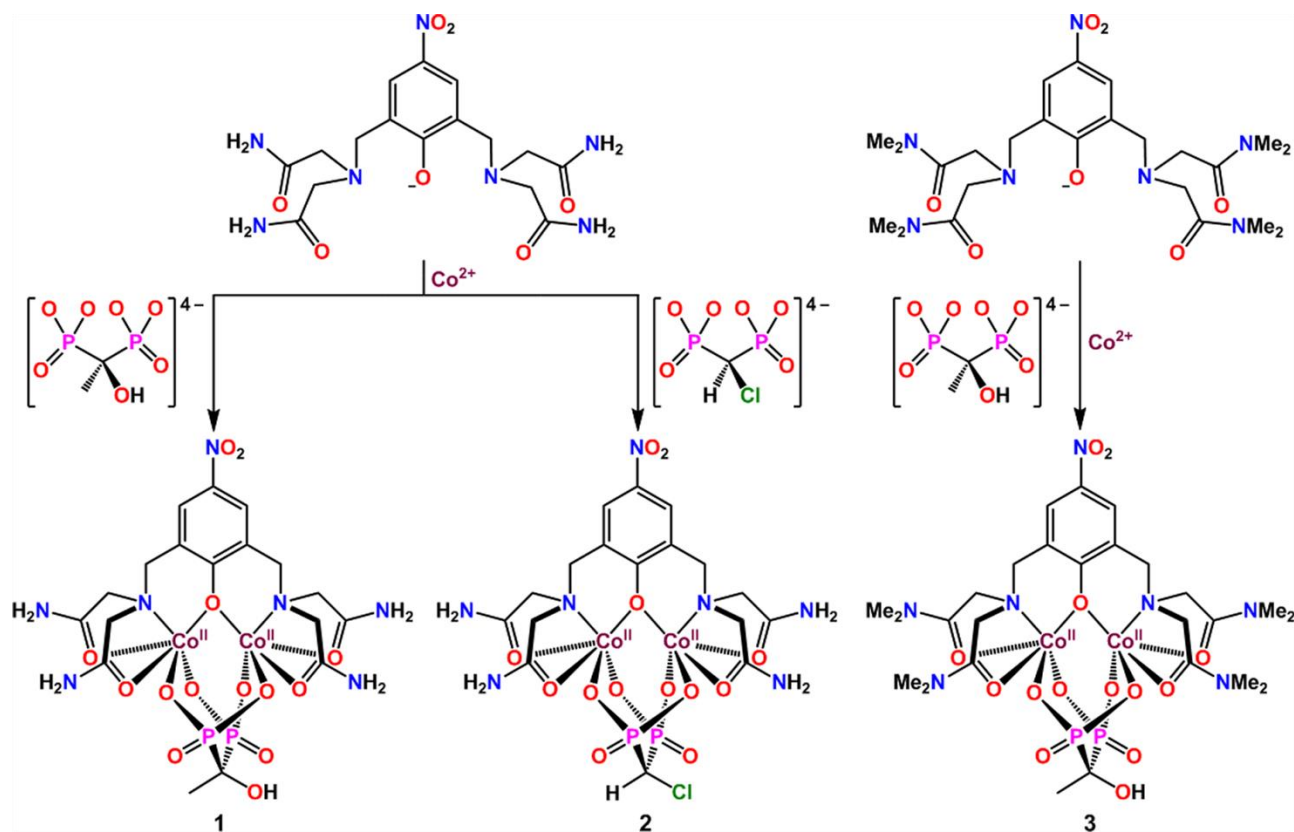


Figure 1. Reaction of L^- , Co^{2+} , and etidronate (left) or CMDP^{4-} (center) to form $[\text{LCo}_2(\text{etidronate})]^-$ or $[\text{LCo}_2(\text{CMDP})]^-$, as observed in **1** and **2**, respectively. Reaction of L^- , Co^{2+} , and etidronate to form $[\text{L}'\text{Co}_2(\text{etidronate})]^-$, as observed in **3** (right).

plate-shaped crystals of $\text{Na}[\text{LCO}_2(\text{etidronate})]\cdot 6.8\text{H}_2\text{O}$ (**1'**) suitable for single-crystal X-ray diffraction analysis.

Synthesis of $\text{Na}[\text{LCO}_2(\text{CMDP})]\cdot 4.5\text{H}_2\text{O}\cdot \text{MeOH}$ (2**).** A pink solution of $\text{Co}(\text{NO}_3)_2\cdot 6\text{H}_2\text{O}$ (67 mg, 0.23 mmol) in MeOH (2 mL) was added dropwise to a stirring yellow suspension of HL (49 mg, 0.11 mmol) in MeOH (3 mL) to give a dark orange solution. A colorless solution of chloromethanediphosphonic acid (H_4CMDP) (27 mg, 0.13 mmol) in MeOH (2 mL) was then slowly added, resulting in a light orange solution. Subsequently, a colorless solution of $\text{Na}(\text{OMe})$ (31 mg, 0.58 mmol) in MeOH (2 mL) was added dropwise to give a light orange suspension. The reaction mixture was stirred at 25 °C for 2.5 h, and then the orange solid was collected by vacuum filtration, washed with MeOH (10 mL) and Et_2O (15 mL), and dried under reduced pressure for 19 h to give **2** (46 mg, 45%) as an orange solid. Anal. Calcd. for $\text{C}_{18}\text{H}_{36}\text{ClCo}_2\text{N}_7\text{NaO}_{18.5}\text{P}_2$: C, 24.43; H, 4.10; N, 11.08%. Found: C, 24.49; H, 3.65; N, 10.74%. ICP-OES: Co:P = 1.02:1.00. UV-Vis absorption spectrum (80 μM ; 50 mM HEPES buffered at pH 7.4, 25 °C): 375 nm ($\epsilon = 14100 \text{ M}^{-1} \text{ cm}^{-1}$). ESI-MS (m/z): Calcd. for $\text{C}_{17}\text{H}_{23}\text{ClCo}_2\text{N}_7\text{O}_{13}\text{P}_2$ ($[\text{LCO}_2(\text{CMDP})]^-$): 747.92, found 747.93; calcd. for $\text{C}_{17}\text{H}_{25}\text{ClCo}_2\text{N}_7\text{O}_{13}\text{P}_2$ ($[\text{LCO}_2(\text{CMDP})+2\text{H}]^+$): 749.93, found 749.89. FT-IR (ATR, cm^{-1}): 3339 (w, broad); 3173 (w, broad); 1663 (s); 1596 (m); 1500 (w); 1447 (m); 1311 (s); 1133 (s); 1097 (s); 911 (m); 878 (w); 799 (w); 752 (m); 688 (m); 662 (m); 529 (s); 475 (s). Slow diffusion of MeCN vapor into a concentrated solution of **2** in H_2O gave dark orange block-shaped crystals of $\text{Na}[\text{LCO}_2(\text{CMDP})]\cdot 8.2\text{H}_2\text{O}$ (**2'**) suitable for single-crystal X-ray diffraction analysis.

Synthesis of $\text{Na}[\text{L}'\text{Co}_2(\text{etidronate})]\cdot 1.2\text{NaNO}_3\cdot 1.9\text{H}_2\text{O}$ (3**).** A pink solution of $\text{Co}(\text{NO}_3)_2\cdot 6\text{H}_2\text{O}$ (54 mg, 0.19 mmol) in MeOH (2 mL) was added dropwise to a stirring yellow solution of HL' (50 mg, 0.093 mmol) in MeOH (2 mL) to give an orange solution. After stirring at 25 °C for 5 min, a colorless solution of etidronic acid monohydrate (21 mg, 0.093 mmol) in MeOH (2 mL) was added dropwise, followed by addition of sodium methoxide (25 mg, 0.46 mmol) in MeOH (2 mL). The resulting orange solution was stirred at 25 °C for 2 h, collected by vacuum filtration, and dried under reduced pressure. The resulting red-orange residue was stirred in MeCN (10 mL) for 15 min and a small amount of white solid was removed by vacuum filtration. The filtrate was dried under reduced pressure, and the ensuing solid was further dried for 16 h to give **3** (92 mg, 97%) as a red-orange solid. Anal. Calcd. for $\text{C}_{26}\text{H}_{45.8}\text{Co}_2\text{N}_{8.2}\text{Na}_{2.0}\text{O}_{19.5}\text{P}_2$: C, 30.74; H, 4.55; N, 11.31%. Found: C, 30.88; H, 4.40; N, 11.52%. ICP-OES: Co:P = 1.01:1.00. UV-Vis absorption spectrum (87 μM ; 50 mM HEPES buffered at pH 7.4, 25 °C): 379 nm ($\epsilon = 12300 \text{ M}^{-1} \text{ cm}^{-1}$). ESI-MS (m/z): Calcd. for $\text{C}_{26}\text{H}_{44}\text{Co}_2\text{N}_7\text{O}_{14}\text{P}_2$ ($[\text{L}'\text{Co}_2(\text{etidronate})+2\text{H}]^+$): 858.11, found 858.11. FT-IR (ATR, cm^{-1}): 3300 (w, broad); 2930 (w); 1612 (s); 1502 (w); 1408 (w); 1297 (s); 1169 (m); 1124 (m); 1061 (s); 896 (m); 809 (w); 751 (w); 688 (w); 645 (w); 542 (s); 462 (s).

X-ray Structure Determination. Single crystals of $\text{Na}[\text{LCO}_2(\text{etidronate})]\cdot 6.8\text{H}_2\text{O}$ (**1'**) and $\text{Na}[\text{LCO}_2(\text{CMDP})]\cdot 8.2\text{H}_2\text{O}$ (**2'**) were directly coated with Paratone-N oil, mounted on a MicroMounts rod, and frozen under a stream of dinitrogen during data collection. The crystallographic data were collected at 100 K on a Bruker Kappa Apex II diffractometer equipped with an APEX-II detector and MoK α sealed tube source. Raw data were integrated and corrected for Lorentz and polarization effects with Bruker

APEX2 version 2014.11-0.¹³ Absorption corrections were applied using the program SADABS.¹⁴ Space group assignments were determined by examining systematic absences, E-statistics, and successive refinement of the structures. Structures were solved using direct methods in SHELXT and refined by SHELXL¹⁵ operated within the OLEX2 interface.¹⁶ All hydrogen atoms were placed at calculated positions using suitable riding models and refined using isotropic displacement parameters derived from their parent atoms. In the crystal structure of **2'**, the Cl atom on the CMDP^{4-} ligand is positionally disordered over two positions. The occupancy of the Cl was freely refined over the two positions. Partially-occupied solvent H_2O molecules not directly bonded to the sodium ions were modeled isotropically. Thermal parameters for all other non-hydrogen atoms were refined anisotropically. Crystallographic data for these compounds at 100 K and the details of data collection are listed in Table S1.

NMR Spectroscopy. ^1H and $^{31}\text{P}\{^1\text{H}\}$ NMR spectra of ligands and organic precursors were collected at 25 °C at 500 and 202 MHz frequencies, respectively, on Agilent DD2 500 MHz (11.7 T) or Varian Inova 500 MHz (11.7 T) spectrometers, or on an automated Agilent DD MR 400 MHz (9.4 T) spectrometer at 400 and 162 MHz frequencies, respectively. $^{13}\text{C}\{^1\text{H}\}$ NMR spectra of ligands were obtained at 25 °C on a Bruker Avance III 500 MHz (11.7 T) system at 126 MHz frequency. Variable-temperature ^1H NMR spectra of compounds **1–3** were collected on Agilent DD2 500 MHz (11.7 T) and Agilent DD2 400 MHz (9.4 T) spectrometers. ^1H NMR spectra of samples in aqueous solutions containing 50 mM HEPES and 100 mM NaCl buffered at various pH values were acquired using D_2O in an inner capillary to lock the sample. Variable-pH ^1H NMR spectra of samples in fetal bovine serum (FBS) were recorded similarly. The pH of commercially available FBS (Fisher Scientific, catalog no. MT35010CV) was adjusted to the desired values by addition of minimal amounts of dilute aqueous nitric acid and sodium hydroxide solutions. Chemical shift values (δ) are reported in ppm and referenced to residual signals from the deuterated solvents (^1H NMR spectra: 7.26 ppm for CDCl_3 , 4.79 ppm for D_2O , and 3.31 ppm for CD_3OD ; $^{13}\text{C}\{^1\text{H}\}$ NMR spectra: 77.16 ppm for CDCl_3 , and 49.00 ppm for CD_3OD). ^{13}C NMR measurements in D_2O were carried out with 5% (v/v) MeOH added as a reference ($\delta = 49.50$ ppm). $^{31}\text{P}\{^1\text{H}\}$ NMR spectra are referenced to an external standard of 85% phosphoric acid solution in D_2O ($\delta = 0$ ppm). For measurements of **1–3** in D_2O or H_2O , the chemical shift of the solvent signal was set to 0 ppm to simplify comparison between ^1H NMR spectra and the corresponding CEST spectra (Z spectra). All coupling constants (J) are reported in Hertz (Hz). The MestReNova 10.0 NMR data processing software was used to analyze and process all recorded NMR spectra. T_1 relaxation times of H_2O were measured after detuning the Agilent DD2 400 MHz instrument to 392 MHz to account for radiation damping, and obtained by fitting H_2O signal intensities from experiments with an array of relaxation times implemented in the program *vnmr*.

Estimation of pK_a by ^1H NMR Analysis. The pH-dependent ^1H NMR chemical shifts of the CH_3 resonance from etidronate for compounds **1** and **3**, and the CH resonance from CMDP^{4-} for **2** were used to estimate the pK_a values of compounds **1–3**. The change in ^1H NMR chemical shift for these resonances as a function of pH was fitted to a Boltzmann sigmoidal function¹⁷ to model a single ionization event according to the following equation:

$$\delta = A_2 + (A_1 - A_2)/(1 + \exp((\text{pH} - \text{pK}_a)/dx)) \quad (1)$$

In this equation, δ is the obtained chemical shift, A_2 is the theoretical chemical shift of the fully deprotonated species, A_1 is the theoretical chemical shift of the fully protonated species, pK_a is the inflection point of the graph, and dx is a parameter describing the steepness of the curve.

CEST Experiments. Variable-temperature CEST experiments were carried out on an Agilent DD2 400 MHz (9.4 T) spectrometer. In a typical CEST experiment, 6–15 mM samples of **1–3** in either an aqueous buffer solution containing 50 mM HEPES and 100 mM NaCl or FBS at desired pH values (measured with a pH electrode immediately before ^1H NMR and CEST data collection) were measured. Z-spectra (CEST spectra) were obtained according to the following protocol: ^1H NMR spectra were acquired from -50 to 130 ppm with a step increase of 1 ppm using a presaturation pulse applied for 6 s at a power level (B_1) of 24 μT . D_2O was placed in an inner capillary within the NMR sample tube to lock the sample. The normalized integrations of the H_2O signal from the obtained spectra were plotted against frequency offset to generate a Z-spectrum. Generally, direct saturation of the H_2O signal was set to 0 ppm, but ± 1 ppm shift was observed for several samples.

Exchange rate constants (k_{ex}) were calculated following a previously reported method,¹⁸ where the x -intercept ($-1/k_{\text{ex}}$) was obtained from a plot of $M_z/(M_0 - M_z)$ (M_z and M_0 are the magnetization of the on- and off-resonance, respectively) against $1/\omega_1^2$ (ω_1 in rad s^{-1}). ^1H NMR spectra were acquired at various presaturation power levels ranging from 10 to 24 μT applied for 6 s at 37 $^\circ\text{C}$. The B_1 values were calculated based on the calibrated 90° pulse on a linear amplifier. To correct for baseline variations, a linear baseline was drawn directly between the first data point (129 – 131 ppm) and the data point at 45 ppm frequency offset. Note that due to poor baseline for the pH 6.62 sample for **2**, a linear baseline correction was applied for each CEST peak by using the data points at 129 and 85 ppm, and at 85 and 45 ppm, respectively. Reported values of %CEST ($(1 - M_z/M_0) \times 100\%$) are the differences in % H_2O signal reduction between applied on-resonance presaturations (raw data) and the values obtained by inserting the corresponding frequencies into the linear baseline equations. To calculate k_{ex} , the CEST intensities at the frequency offsets corresponding to maximum H_2O signal reductions at 24 μT power level were monitored for each pH value. The pH calibration curves were generated by taking the base 10 logarithm of the ratios of two CEST signal intensities (reported as $M_0/M_z - 1$)^{9c-e,19,20} after a baseline correction was applied.

Solution Magnetic Measurements. The solution magnetic moments of compounds **1–3** were determined using the Evans method,²¹ by collecting variable-pH ^1H NMR spectra at 37 $^\circ\text{C}$ (310 K) on an Agilent DD2 500 MHz (11.7 T) spectrometer. In a typical experiment, the compound (3 – 7 mM) was dissolved in a mixture of 2% (v/v) *tert*-butanol in an aqueous solution containing 50 mM HEPES and 100 mM NaCl buffered at a specific pH value. The resulting solution was placed in an NMR tube containing a sealed capillary with the same solvent mixture but without the to-be-characterized paramagnetic compound as a reference solution. Diamagnetic corrections were carried out based on the empirical formula of each compound (as determined by elemental analysis) using Pascal's constants.²² The paramagnetic molar susceptibility $\chi_{\text{M}}^{\text{para}}$ ($\text{cm}^3 \text{mol}^{-1}$) was calculated using the following equation:²¹

$$\chi_{\text{M}}^{\text{para}} = (3\Delta\nu M_w)/(4\pi\nu_0 m) - \chi_{\text{M}}^{\text{dia}} \quad (2)$$

In this equation, $\Delta\nu$ is the frequency difference (Hz) between the *tert*-butyl resonance of *tert*-butanol in the sample and reference solutions, M_w is the molecular mass of the paramagnetic compound (g mol^{-1}), ν_0 is the operating frequency of the NMR spectrometer (Hz), m is the concentration of the paramagnetic compound (g cm^{-3}), and $\chi_{\text{M}}^{\text{dia}}$ is the diamagnetic contribution to the molar susceptibility ($\text{cm}^3 \text{mol}^{-1}$).

UV-Visible Absorption Spectroscopy. Solution and solid-state UV-Visible spectra were collected in the 200 – 800 nm range on an Agilent Cary 5000 UV-Vis-NIR spectrometer equipped with an integrating sphere for diffuse reflectance measurements. Solution spectra were collected on 64 – 87 μM samples of compounds **1–3** in aqueous buffer solutions containing 50 mM HEPES and 100 mM NaCl in the pH range used for CEST experiments. Diffuse reflectance spectra were collected on crystalline samples of **1'** and **2'**. Samples were prepared by grinding single crystals of the compounds, followed by mixing with BaSO_4 powder for a two-fold dilution.

Electrochemical Measurements. Cyclic voltammetry measurements were carried out in a standard one-compartment cell under dinitrogen using CH Instruments 760c potentiostat. The cell consisted of a glassy carbon as a working electrode, a platinum wire as a counter electrode, and a saturated calomel electrode (SCE) as a reference electrode. Analytes were measured in aqueous solutions with 100 mM NaCl and 50 mM HEPES buffered at pH 7.4. All potentials were converted and referenced to the normal hydrogen electrode (NHE), using a literature conversion factor.²³

Other Physical Measurements. Preparative reverse-phase HPLC was performed on a Waters 19×250 mm² XBridge C18 column, using a Varian Prostar 500 system equipped with a Varian 363 fluorescence detector and a Varian 335 UV-Vis detector. During HPLC experiments, H_2O was used as solvent A and MeCN as solvent B. The absorbances at 220 and 285 nm were monitored. The electrode-based pH measurements were carried out using a Thermo Scientific Orion 9110DJWP double junction pH electrode connected to a VWR sympHony B10P pH meter. The pH meter was calibrated using standardized pH buffer solutions at 4.01 , 7.00 , and 10.00 purchased from LaMotte Company. Elemental analysis was conducted by Midwest Microlab Inc. Infrared spectra were recorded for solid samples of **1–3** on a Bruker Alpha FTIR spectrometer equipped with an attenuated total reflectance accessory. These data are provided in Figure S1. Electrospray ionization mass spectrometry (ESI-MS) measurements were performed on a LC-MS Bruker AmaZon X quadrupole ion trap instrument, equipped with a Compass software version 1.4. All measurements were carried out in MeOH carrier solvent using positive and/or negative ionization mode. Inductively-coupled plasma optical emission spectroscopy (ICP-OES) was performed on a Thermo iCAP 7600 dual view ICP-OES instrument equipped with a CETAC ASX520 240-position autosampler. Samples were dissolved in a 3% aqueous nitric acid solution and the emissions for Co and P compared to standard solutions.

Cell Viability Measurement. Melanoma B16F10 cells were purchased from American Type Culture Collection and cultured in Dulbecco's Modified Eagle's Media (Life Technologies) with 10% (v/v) FBS (Fisher Scientific), 1 mM sodium pyruvate (Sigma Aldrich), 0.1 mM non-essential amino acids (Sigma Aldrich), and 4 mM of L-glutamate. Cells were grown in a humidified incubator operating at 37 $^\circ\text{C}$ and 5.0% CO_2 , and harvested by incubation with 0.25% TrypLE for 5

min at 37 °C in a 5.0% CO₂ incubator. Cells for the experiment were sub-cultivated twice after thawing the cell stocks. B16F10 cells were seeded at a density of 25,000 cells per well in a 24-well plate and allowed to grow for 24 h before incubation. Cells were incubated with media containing concentrations of **1** ranging from 0.2–11.3 mM (300 μL, 7 concentrations) for 24 h before viability measurements were carried out. The stock solution of **1** was filtered with a 0.2 μm sterile filter prior to incubation with the cells. Cell viability was measured using a Guava easyCyte HT flow cytometer equipped with a 96-well plate/10 tube autosampler (EMD Millipore). Each sample subjected for analysis contained 50 μL of a well-mixed cell suspension in phosphate buffered saline (PBS) and 150 μL of Guava ViaCount reagent. Samples were transferred to a 96-well plate and immediately counted using the Guava ViaCount software module. Viability was measured using the EasyFit Analysis feature. Attempts to use cells not treated with **1** as a control to estimate normal cell death remained unsuccessful. For that reason, cell viability (in %) is reported without taking normal cell death into account. Therefore, the reported viability corresponds to the lower limit of cell survival at each concentration of **1**. Note, however, that we observed a considerable number of dead cells in the control solution not treated with **1**, even though this number could not be accurately quantified.

MRI Phantom Experiments. Samples for phantom experiments contained 17 mM of **1** in aqueous solutions with 50 mM of HEPES and 100 mM of NaCl buffered at selected pH values ranging from 6.40 to 7.88. All samples were filtered through a 0.22 μm nylon membrane, transferred to borosilicate glass capillaries (0.2 mm thickness, 1.5–1.8 mm outer diameter), and flame sealed. A bundle of 10 capillaries, each containing a solution of **1** buffered at a specific pH, was placed within an NMR tube (18 mm outer diameter) filled with an aqueous solution containing 1 mM gadodiamide (Omniscan) for T₁ matching. CEST experiments were carried out on an 89 mm vertical bore Bruker Avance III HD 750 MHz (17.6 T) MRI scanner running ParaVision 6.0.1 (Bruker Biospin, Billerica, MA, USA). Temperature was maintained at 37 °C using heated water flowing through the gradient coils. The probe and samples were allowed to equilibrate at this temperature for 1 h before acquisition. CEST images were acquired using a standard spin echo imaging sequence with presaturation pulses (74.3 μT, 570 ms total duration) consisting of a train of 1250 Gaussian pulses, each of 0.44 ms (6.2 kHz bandwidth), applied at 64 and 104 ppm frequency offsets (*M_z*), respectively. Other imaging acquisition parameters were as follows: field of view (FOV) = 15 × 15 mm²; matrix = 256 × 256; repetition time (TR) = 2000 ms; echo time (TE) = 3.75 ms; flip angle = 210°; slice thickness = 2 mm; averages = 3. Reference unsaturated images were acquired at 0 ppm frequency offset (*M₀*) using identical parameters except the pulse amplitude was set to 0 μT. Due to a slight difference in observed chemical shift (ca. 1 ppm) between the H₂O signals in the capillaries and the surrounding solution, 0 ppm was defined as the H₂O signal in the capillary tubes. To reduce chemical shift artifacts in the images, 1.2 kHz bandwidth excitation and refocusing pulses were used in the spin echo sequence. A sine smoothing filter was applied to the raw k-space data to remove Gibbs ringing artifacts in the images.

All images were produced in MATLAB R2016b version 9.1.0 (The MathWorks Inc., Natick, MA, USA). Custom scripts were written in MATLAB to calculate the CEST images, CEST_{104 ppm}/CEST_{64 ppm} ratios, and to apply the pH calibration

to produce pH maps of the samples. Gating images were produced to remove noise from the remainder of the images, as well as signals from the surrounding doped H₂O. These were generated from binary gating images acquired with no saturation pulses, and dedicated images suppressing signals from only the capillaries. The difference between these produces binary gating images of just the capillary tubes. An image erosion routine was used to shrink these images to the central region of the capillary tubes (75.4% of the total cross-sectional area), to remove unwanted partial volume and susceptibility effects. These central regions were used for CEST data analysis and are shown in Figure 6. Values of %CEST are reported as %CEST = (1 – *M_z*/*M₀*) × 100%. Averaged intensities of the regions shown in Figure 6 (upper) were employed to calculate the CEST_{104 ppm}/CEST_{64 ppm} ratios and the corresponding log₁₀(CEST_{104 ppm}/CEST_{64 ppm}) values used to generate the pH calibration curve between pH 6.58 and 7.54. Note that for both the CEST intensity ratios and the pH calibration curve, the CEST signal intensities are reported as *M₀*/*M_z* – 1,^{9c-e,19,20} in analogy to the data obtained from NMR measurements.

RESULTS AND DISCUSSION

Syntheses and Structures. The nitro-substituted tetra(carboxamide) chelating ligand HL was selected as a CEST-active ligand, and its permethylated analogue HL' was selected as a CEST-inactive counterpart. These ligands were synthesized through S_N2 reactions between 2,2'-iminobis(acetamide) derivatives and 2,6-bis-(bromomethyl)-4-nitrophenol (see experimental details and Schemes S1 and S2 in the Supporting Information). Reaction of the ligands with two equivalents of Co(NO₃)₂·6H₂O and one equivalent of etidronic or chloromethanediphosphonic acid (H₄CMDP) in MeOH, in the presence of five equivalents of Na(OMe), afforded compounds Na[LCO₂(etidronate)]·0.2NaNO₃·2.7H₂O (**1**), Na[LCO₂(CMDP)]·4.5H₂O·MeOH (**2**), and Na[L'CO₂(etidronate)]·1.2NaNO₃·1.9H₂O (**3**) as orange solids (see Experimental Section and Figure 1). The ancillary ligand etidronate was selected based on the potential for the hydroxyl group to exhibit the CEST effect. The related ligand CMDP⁴⁻ was prepared to serve as an analogous ancillary ligand with no exchangeable protons, as the two bisphosphonates feature

Table 1. Selected Mean Interatomic Distances (Å) and Angles (°) in **1'** and **2'** at 100 K

	1'	2'
Co–O _{phenoxo}	2.0920(2)	2.0913(2)
Co–O _{amide}	2.1127(1)	2.1044(1)
Co–O _{phosphonate}	2.0618(1)	2.0684(1)
Co–N	2.1558(2)	2.1578(2)
Co···Co	3.6740(3)	3.6780(3)
Co–O _{phenoxo} –Co	122.837(4)	123.136(5)
O–P–O	113.882(3)	113.993(4)
P–C–P	111.486(6)	112.901(6)
trans O–Co–E ^a	170.324(1)	170.451(1)
Σ _{sum} ^b	62.27(2)	62.83(2)
Σ _{mean}	5.19(1)	5.24(1)
ω ^c	49.120(4)	49.260(4)

^aE denotes either a N or an O atom from the [CoNO₅] coordination sphere. ^bOctahedral distortion parameter (Σ) = absolute deviation from 90° of each 12 cis angle in [CoNO₅]. ^cDihedral angle between the Co–O_{phenoxo}–Co plane and the plane of the phenolate ring of L[–].

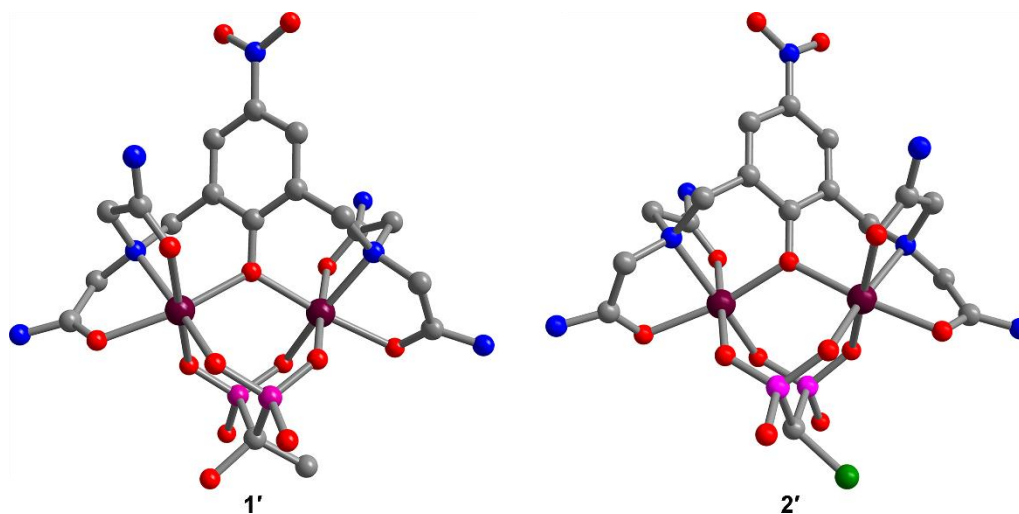


Figure 2. Crystal structures of the anionic complexes $[\text{LCo}_2(\text{etidronate})]^-$ (left) and $[\text{LCo}_2(\text{CMDP})]^-$ (right), as observed in **1'** and **2'**, respectively. Purple, green, magenta, red, blue, and gray spheres represent Co, Cl, P, O, N, and C atoms, respectively; H atoms are omitted for clarity.

similar steric and electronic properties.

Slow diffusion of MeCN vapor into a concentrated solution of **1** and **2** in H_2O afforded plate- and block-shaped crystals of $\text{Na}[\text{LCo}_2(\text{etidronate})]\cdot 6.8\text{H}_2\text{O}$ (**1'**) and $\text{Na}[\text{LCo}_2(\text{CMDP})]\cdot 8.2\text{H}_2\text{O}$ (**2'**), respectively. Single-crystal X-ray diffraction analysis at 100 K revealed that **1'** and **2'** are isostructural and crystallize in the monoclinic space group $P2_1/n$, with one anionic Co_2 complex and one Na^+ ion constituting the asymmetric unit (see Table S1). In each complex, the two nearly identical Co centers reside in distorted octahedral coordination environments, each comprised of a μ -phenoxo oxygen atom, a tertiary amine nitrogen atom, and two carboxamide oxygen atoms from L^- . The remaining two coordination sites are occupied by oxygen atoms from the bridging bisphosphonate, which coordinates the metal ions in a $\mu^2\text{-}\kappa^4$ binding mode (see Figure 2). The hexagonal plane of the aromatic ring of L^- and the trigonal plane defined by the two Co centers and the μ -phenoxo oxygen atom are twisted relative to another, with dihedral angles of $49.120(4)^\circ$ and $49.260(4)^\circ$ for **1'** and **2'**, respectively (see Table 1).

The mean Co–O bond distances range from $2.0618(1)$ to $2.1127(1)$ Å in **1'**, and from $2.0684(1)$ to $2.1044(1)$ Å in **2'**. In comparison, the slightly longer mean Co–N bond lengths of $2.1558(2)$ and $2.1578(2)$ Å for **1'** and **2'**, respectively, reflect weaker coordination of the tertiary amines to the metal centers due to steric conflicts. These mean bond distances, in conjunction with the average deviations from 90° observed in the bond angles for the 12 cis angles in the $[\text{CoNO}_5]$ coordination sphere of $5.19(1)$ and $5.24(1)^\circ$ for **1'** and **2'**, respectively, are consistent with a high-spin Co^{II} electronic configuration.^{24,25} Furthermore, the intramolecular $\text{Co}\cdots\text{Co}$ distance and Co–O_{phenoxo}–Co angle of $3.6740(3)$ Å and $122.837(4)^\circ$ for **1'** and $3.6780(3)$ Å and $123.136(5)^\circ$ for **2'** are consistent with related phenoxo-bridged Co^{II}_2 complexes.^{24,25} Finally, the similar O–P–O and P–C–P bond angles for the etidronate and CMDP⁴⁻ ancillary ligands in **1'** and **2'**, respectively, verify the insignificant structural changes associated with altering the ancillary bisphosphonate. Taken together, these comparable structural metrics for **1'** and **2'** provide validation for the use of CMDP⁴⁻ as a CEST-inactive analogue of etidronate.

UV-Vis Spectroscopy. To probe the electronic structure of compounds **1–3** in solution, UV-Visible absorption spectra

were collected for samples in aqueous buffer solutions containing 50 mM HEPES and 100 mM NaCl. The spectrum for a sample of **1** buffered at pH 7.4 features a strong absorption at 375 nm ($\epsilon = 13800 \text{ M}^{-1} \text{ cm}^{-1}$) (see Figure S2). Similarly, a solution of **2** shows a nearly identical absorption band at this wavelength ($\epsilon = 14100 \text{ M}^{-1} \text{ cm}^{-1}$) under the same conditions (see Figure S3). Based on these observations and literature precedent for similar phenoxo-bridged Co_2 complexes,^{24c,25a} we assign these absorptions to ligand–metal charge transfer (LMCT) transitions from the phenolate to Co^{II} . The close similarity of the spectrum for **3** in pH 7.4 buffer, which exhibits a single intense band at 379 nm ($\epsilon = 12300 \text{ M}^{-1} \text{ cm}^{-1}$), further supports the assignments of these spectral features (see Figures S4 and S5). Notably, both the positions and intensities of the absorption bands are relatively unaffected by pH between 5.8 and 8.3 (see Figures S2–S4). Furthermore, the diffuse reflectance spectra collected for crystalline solid-state samples of **1'** and **2'** feature peaks with maxima at 379 and 376 nm, respectively (see Figures S6 and S7). These data indicate that the structures of $[\text{LCo}_2(\text{etidronate})]^-$ and $[\text{LCo}_2(\text{CMDP})]^-$ determined from X-ray diffraction analysis are preserved in aqueous HEPES solutions in the physiological pH range.

Solution Magnetic Properties. To assess the magnetic behavior of the three Co_2 complexes, dc magnetic susceptibility data were obtained at 37°C for aqueous buffer solutions in the pH range 5.8–8.4 using the Evans method²¹ (see Experimental Section). The resulting plots of $\chi_{\text{M}}T$ vs pH are shown in Figures S8–S10. For all compounds, $\chi_{\text{M}}T$ varies insignificantly with pH, affording average values of $\chi_{\text{M}}T = 6.3(3)$, $6.0(2)$, and $6.1(2) \text{ cm}^3 \text{ K mol}^{-1}$ for **1**, **2**, and **3**, respectively (see Table S2). The mean magnetic moments per Co^{II} site correspond to g values ranging from 2.5(1) to 2.6(1), indicative of a significant contribution from orbital angular momentum to the magnetic moments of **1–3**. These data are in accord with the high magnetic anisotropy of octahedral, $S = 3/2$ Co^{II} centers,^{12a} and agree with values reported for structurally similar high-spin Co^{II}_2 complexes.²⁴ In sum, the magnetic properties of **1–3** are nearly identical in aqueous solution within the physiologically relevant pH range at 37°C .

NMR Spectroscopy. To further examine and compare the solution properties of the Co_2 complexes, ^1H NMR spectra

were collected for aqueous solutions of **1–3** buffered at selected pH values. All compounds gave sharp, well-resolved NMR spectra, consistent with high-spin Co^{II} ions in pseudo-octahedral geometry.¹² The spectrum for **1** at pH 7.18 features 22 paramagnetically shifted resonances that range in chemical shift from -110 to 185 ppm vs H_2O (see Figure S11, upper). The resonances at 9.5, 13, 64, 68, 102, 104, and 105 ppm are assigned to exchangeable protons on the carboxamide groups and the etidronate hydroxyl group, as evidenced by their disappearance in the analogous spectrum recorded in neutral D_2O (see Figure S11, lower). The anticipated two additional amide resonances are most likely concealed by the broad H_2O signal. The appearance of the 22 NMR signals as 10 pairs of closely spaced peaks is consistent with the pseudo- C_2 symmetry of $[\text{LCo}_2(\text{etidronate})]^-$ in **1**, where a slight lowering from C_2 results from the asymmetry of the etidronate ligand. The two remaining peaks correspond to the hydroxyl and methyl substituents on etidronate. Upon raising the pH from 6.18 to 8.14, the exchangeable proton resonances become significantly more broad, indicative of faster proton exchange (see Figure S12).

In comparison, the spectrum for **2** at pH 7.18 exhibits 23 paramagnetically shifted peaks in the range -105 – 180 ppm vs H_2O , with exchangeable carboxamide signals at 4.7, 6.8, 9.5, 11, 68, 70, 102, and 104 ppm, verified by comparison of the spectra recorded in H_2O and D_2O (see Figure S13). Notably, the presence of four highly-shifted amide resonances that are well separated from the four remaining amide peaks confirms the inequivalency of the two amide NH protons due to restricted C–N bond rotation.²⁶ This inequivalence is a common observation for amide-appended transition metal complexes.^{9f,11a–11j,26ac} The close similarity between the spectra for **1** and **2** (see Figure S14) suggests that these compounds are structurally similar in solution, as observed in the solid-state. The replacement of the intense peak at 66 ppm in the spectrum for **1** with a peak at 138 ppm in the spectrum for **2** indicates that these signals correspond to the CH_3 and CH resonances from the etidronate and CMDP⁴⁻ ancillary ligands, respectively. Moreover, the linewidths of the carboxamide peaks for **2** show similar pH dependence between pH 6.62 and 8.34, as observed for **1** (see Figure S15).

In analogy to the ^1H NMR features of the Co_2 complexes of L^- , the resonances in the spectrum for **3** at pH 7.47 span from -110 to 190 ppm vs H_2O and display a similar spectral profile (see Figure S16). The intense peaks at -9.8 , -7.5 , -3.7 , 1.6 , 2.0 , 22 , and 26 ppm are assigned to methyl groups on L'^- , and the CH_3 resonance from etidronate is observed at 62 ppm. Furthermore, comparison of the spectra recorded in pH 8.08 buffer and slightly basic D_2O reveals the disappearance of the peak at 103 ppm (see Figure S17). This observation indicates that the etidronate hydroxyl group provides a well-resolved NMR signal under basic conditions, and further corroborates the presence of three exchangeable proton resonances for **1** in the 102–105 ppm range. Upon lowering the pH to 5.80, the hydroxyl peak for **3** undergoes significant line broadening, suggesting an increase in the proton exchange rate (see Figure S18). Importantly, inspection of the NMR linewidths of the carboxamide peaks for **1** and **2** and the hydroxyl resonance for **3** implies opposing pH dependences of the proton exchange rates for these two functional groups, and therefore highlights the potential utility of **1** for ratiometric pH imaging.

CEST Properties. In order to investigate the feasibility of employing **1** as a pH-responsive PARACEST probe, CEST spectra were collected for aqueous solutions containing 12.8

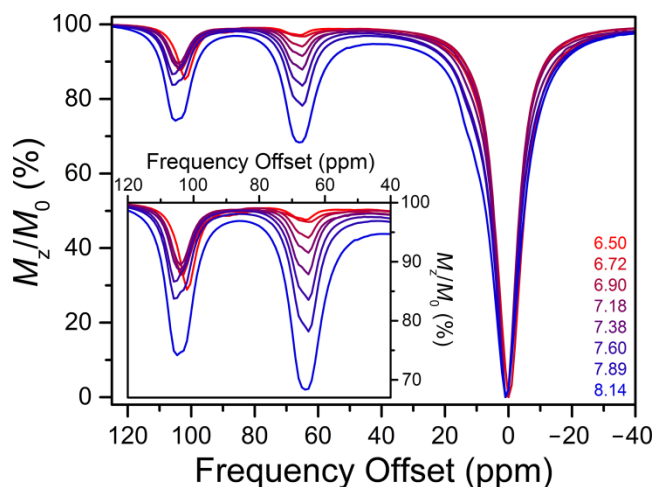


Figure 3. CEST spectra collected at 37 °C for 12.8 mM aqueous solutions of **1** with 50 mM HEPES and 100 mM NaCl buffered at pH 6.50–8.14 (red to blue). The legend gives the pH and corresponding color of each sample. Inset: Expanded view of the CEST peaks of interest.

mM of **1** with 50 mM HEPES and 100 mM NaCl buffered at pH values ranging from 6.50 to 8.14 (see Figure 3). The spectrum at pH 6.50 exhibits two peaks, centered at 66 and 102 ppm, with 2.0 and 14% H_2O signal reduction, respectively. Note that CEST signals from the labile protons below 13 ppm are masked by direct saturation of the H_2O solvent. As the pH is raised to 8.14, the CEST peak at 66 ppm shifts to 64–65 ppm, and the intensity increases monotonically to 27%. This increase in CEST intensity with pH is consistent with base-catalyzed proton exchange that is typical for carboxamides.^{9af,11ad–11h,20}

In stark contrast, the CEST effect of the downfield-shifted peak shows a very different pH profile. First, the frequency corresponding to maximum CEST intensity is markedly affected by pH variations and shifts from 102 to 106 ppm in the pH range 6.50–8.14. Surprisingly, the CEST intensity remains relatively constant between pH 6.50 and 7.60, but then undergoes a significant increase when the pH is raised further. The dramatically different pH dependences of the two CEST features for **1** are evident from a plot of the CEST intensities at 64 and 104 ppm vs pH (see Figure S19). We hypothesize that the unusual CEST behavior at 104 ppm stems from contributions of overlapping carboxamide and hydroxyl resonances to the observed CEST effect, as suggested by ^1H NMR analysis.

To better understand the causes for the unusual CEST properties of **1**, analogous variable-pH CEST spectra were collected for aqueous solutions containing 12 mM of **2** or 13 mM of **3**. The spectra for **2** in the pH range 6.62–8.34 show two peaks at 68 and 102 ppm with CEST intensities that increase significantly when the pH is raised (see Figure S20), similar to that observed for the peak at ca. 64 ppm for **1**. Importantly, the nearly identical pH dependences of the two CEST effects for **2** (see Figure S21) supports the hypothesis that the unique CEST behavior of **1** can be attributed to the etidronate hydroxyl group. Indeed, CEST spectra for **3** obtained between pH 5.80 and 8.08 confirm the PARACEST activity of the ancillary etidronate, as a single peak that shifts from 94 to 103 ppm is observed (see Figure S22). The nature of this pH-induced shift in CEST frequency is discussed below. In conjunction with this frequency shift, the hydroxyl CEST signal undergoes a significant decrease in intensity with

increasing pH, after reaching a maximum intensity of 20% at pH 6.11 (see Figure S23). The observation of optimal CEST under slightly acidic conditions is consistent with PARACEST agents bearing alcohol donors.^{11f,27} Interestingly, all previously reported PARACEST agents with CEST-active hydroxyl protons feature OH groups directly bonded to the metal center.^{9bg,11f,27,28} This further demonstrates the remarkably high CEST peak shift and intensity of the ancillary hydroxyl group in **1** and **3**.

The proton exchange rates at 37 °C were estimated by employing the Omega plot method.¹⁸ The rate constants (k_{ex}) for the amide protons in **2** increase from $2.7(2) \times 10^2$ (68–69 ppm) and $3.5(3) \times 10^2$ (102 ppm) s^{-1} at pH 6.62 to $1.0(1) \times 10^3$ (68–69 ppm) and $8.0(3) \times 10^2$ (102 ppm) s^{-1} at pH 8.34 (see Figures S24–S26 and Table S3). These values are consistent with rates reported for mono-^{9f,11ad–fhj} and dinuclear^{11lm} transition metal PARACEST agents bearing pendent carboxamides. In contrast, the hydroxyl proton exchange in **3** is fastest at pH 5.80 ($k_{\text{ex}} = 1.5(1) \times 10^3 \text{ s}^{-1}$), and then decreases sharply as the pH is raised to 7.47 ($k_{\text{ex}} = 2.5(2) \times 10^2 \text{ s}^{-1}$) (see Figures S27 and S28, and Table S4). The opposite pH trends for exchange rates in **2** and **3** are in accord with ¹H NMR and CEST data, and reflect the base- and acid-catalyzed exchange of the NH and OH protons, respectively, in these Co₂ complexes. To compare, the rate constants for the two CEST features of **1** are similar to those for **2** and **3**, with values of $2.1(3)–7.3(3) \times 10^2$ (64–66 ppm) and $2.8(2)–7.6(3) \times 10^2$ (101–106 ppm) s^{-1} in the pH range 6.18–8.14 (see Figures S29–S31 and Table S5). Note that the pH-dependent changes of the rate constants for **1** are less obvious than those observed for **2** and **3**. Most likely, this difference results from asymmetric CEST peaks for **1** and the contribution of both NH and OH protons to the CEST effect at 101–106 ppm. Therefore, more elaborate methods are needed to accurately determine the exchange rate for each CEST effect of **1**.

Ratiometric CEST Analysis. To assess the potential of compound **1** to enable ratiometric pH quantitation, the pH dependence of the ratio of CEST intensities at 104 and 64 ppm ($\text{CEST}_{104 \text{ ppm}}/\text{CEST}_{64 \text{ ppm}}$) was investigated. Remarkably, the data reveal a substantial decrease in the intensity ratio from a value of 8.35 to 0.82 in the pH range 6.50–7.60, while no significant change is observed at higher pH (see Figure 4). Moreover, the logarithm (\log)²⁹ of this ratio was found to vary linearly with pH in this range (see Figure 4, inset), according to the following equation:

$$\log(\text{CEST}_{104 \text{ ppm}}/\text{CEST}_{64 \text{ ppm}}) = -0.99 \times \text{pH} + 7.4 \quad (3)$$

Conversely, the analogous ratio of CEST intensities at 102 and 68 ppm ($\text{CEST}_{102 \text{ ppm}}/\text{CEST}_{68 \text{ ppm}}$) for **2** is relatively unaffected by pH changes, with values of 0.57–0.98 between pH 6.62 and 8.34 (see Figure 4). This comparison highlights the essential role of the etidronate hydroxyl group to enable ratiometric quantitation of pH in the physiological range with **1**, using Equation 3 as a calibration curve. The slope of a linear calibration curve provides a useful measure of probe sensitivity. Notably, the absolute value of $0.99(7) \text{ pH unit}^{-1}$ obtained for **1** is ca. 2–4-fold greater than those reported for related ratiometric PARACEST pH probes at 37 °C, even when compared to instances where the CEST intensity ratios are employed directly.^{7ac,9c–f}

To further evaluate the efficacy of **1** as a ratiometric pH probe, we first sought to determine whether this pH calibration curve is affected by the concentration of the probe, since a concentration-independent measure is critical for physiologi-

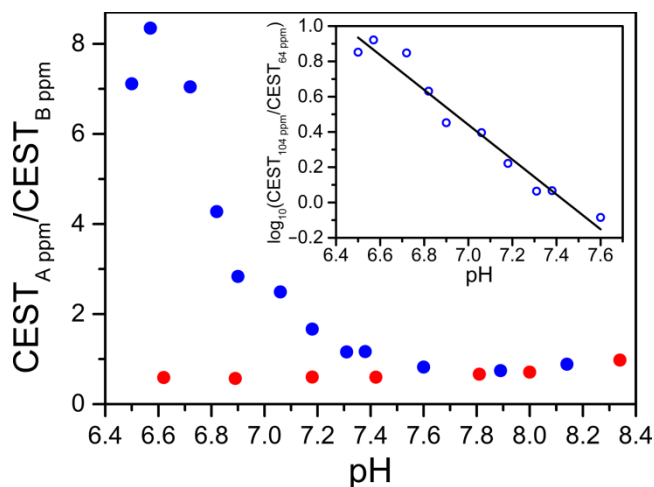


Figure 4. Ratios of CEST intensities ($\text{CEST}_{A \text{ ppm}}/\text{CEST}_{B \text{ ppm}}$) from presaturation at 104 (A) and 64 (B) ppm for 12.8 mM aqueous buffer solutions of **1** (blue), and at 102 (A) and 68 (B) ppm for 12 mM solutions of **2** (red) vs pH. Inset: Semilog form of the plot for **1**. Circles denote experimental data, and the black line corresponds to a linear fit of the data.

cal applications. Toward this end, CEST spectra for aqueous buffer solutions containing 6.4 and 8.5 mM of **1** were recorded analogously to the 12.8 mM sample (see Figures S32 and S33). The CEST effects at 64 and 104 ppm did not vary significantly with different probe concentrations (see Figures S34–S37). This observation suggests that the spin-lattice relaxation rate of H₂O is close to the proton exchange rates within this concentration range,^{6ef,9dh,30} consistent with T_1 analysis (see Table S6). Most importantly, these experiments show that plots of $\text{CEST}_{104 \text{ ppm}}/\text{CEST}_{64 \text{ ppm}}$ vs pH are nearly identical for the three concentrations in the pH range 6.50–8.15 (see Figures S38–S40). Indeed, linear fits of the corresponding $\log(\text{CEST}_{104 \text{ ppm}}/\text{CEST}_{64 \text{ ppm}})$ values as a function of pH afforded the following equations (see Figures S38 and S39, insets):

$$6.4 \text{ mM: } \log(\text{CEST}_{104 \text{ ppm}}/\text{CEST}_{64 \text{ ppm}}) = -1.05 \times \text{pH} + 7.9 \quad (4)$$

$$8.5 \text{ mM: } \log(\text{CEST}_{104 \text{ ppm}}/\text{CEST}_{64 \text{ ppm}}) = -1.03 \times \text{pH} + 7.7 \quad (5)$$

The pH calibration curves obtained for various concentrations of **1** (Equations 3–5) are summarized in Figure S41. For a given $\log(\text{CEST}_{104 \text{ ppm}}/\text{CEST}_{64 \text{ ppm}})$ value, the deviation in pH was found to be ca. 0.02–0.09 pH units over the pH range 6.50–7.60. This observation demonstrates the ability of **1** to quantitate solution pH in a concentration-independent manner within the error of 0.1 pH unit.

Temperature Effects. An important challenge facing pH-responsive MR probes is the ability to deconvolute pH responses from temperature effects of the CEST peak frequency and intensity, owing to the temperature dependences of hyperfine shifts¹² and proton exchange rates.⁹ To examine how temperature variation affects the pH calibration curve, variable-pH ¹H NMR and CEST spectra were collected at the additional temperatures 35 and 39 °C on 12.8 mM solutions of **1** buffered at pH 6.50–8.14. The data show very similar pH-dependent behavior as observed at 37 °C (see Figures S42–S45), albeit with nearly all resonances shifted by ca. 1 ppm away and toward the H₂O signal at 35 and 39 °C, respectively (see Figure S46), consistent with Curie behavior of high-spin Co^{II}.¹² Upon increasing the temperature from 35 to 39 °C, a moderate increase in CEST intensities at 64 and 104 ppm was observed (see Figures S47–S50). Importantly, temperature

changes do not affect the $\text{CEST}_{104 \text{ ppm}}/\text{CEST}_{64 \text{ ppm}}$ values above pH 7.0. In contrast, temperature changes cause significant deviations in the pH profile of $\text{CEST}_{104 \text{ ppm}}/\text{CEST}_{64 \text{ ppm}}$ below pH 7.0 (see Figures S51–S53). Here, fits of the $\log(\text{CEST}_{104 \text{ ppm}}/\text{CEST}_{64 \text{ ppm}})$ vs pH plots using data from the pH range 6.50–7.60 gave the following linear equations (see Figures S51 and S52, insets):

$$35\text{ }^{\circ}\text{C}: \log(\text{CEST}_{104 \text{ ppm}}/\text{CEST}_{64 \text{ ppm}}) = -1.19 \times \text{pH} + 8.9 \quad (6)$$

$$39\text{ }^{\circ}\text{C}: \log(\text{CEST}_{104 \text{ ppm}}/\text{CEST}_{64 \text{ ppm}}) = -0.79 \times \text{pH} + 5.9 \quad (7)$$

The significant effect of temperature variations on the pH calibration curve is primarily due to the temperature-induced shifts in CEST frequencies (see Figure S54). Indeed, fits of the $\log(\text{CEST}_{105 \text{ ppm}}/\text{CEST}_{65 \text{ ppm}})$ and $\log(\text{CEST}_{103 \text{ ppm}}/\text{CEST}_{63 \text{ ppm}})$ vs pH plots for the data obtained from pH 6.50–7.60 at 35 and 39 $^{\circ}\text{C}$, respectively, provided excellent linear correlations following the equations:

$$35\text{ }^{\circ}\text{C}: \log(\text{CEST}_{105 \text{ ppm}}/\text{CEST}_{65 \text{ ppm}}) = -1.06 \times \text{pH} + 7.8 \quad (8)$$

$$39\text{ }^{\circ}\text{C}: \log(\text{CEST}_{103 \text{ ppm}}/\text{CEST}_{63 \text{ ppm}}) = -0.95 \times \text{pH} + 7.1 \quad (9)$$

The calibration curves represented by Equations 8 and 9 closely resemble that obtained at 37 $^{\circ}\text{C}$ (see Figure S55), demonstrating that the %CEST at 105 and 65 ppm, and at 103 and 63 ppm, should be employed for pH measurements at 35 and 39 $^{\circ}\text{C}$, respectively. One potential route to address temperature heterogeneity in physiological environments with this Co_2 probe could involve constructing multiple pH calibration curves, one at each temperature, and then determine the surrounding temperature independently by exploiting the ^1H NMR chemical shift of a resonance that shifts insignificantly with pH. Such simultaneous quantitation of pH and temperature using PARACEST probes has been reported.^{8,9bgh}

Complex Stability and Biocompatibility Studies. The cyclic voltammogram collected for an aqueous solution of **1** in HEPES buffer at pH 7.4 exhibits an irreversible oxidation process at ca. 560 mV vs NHE (see Figure S56). We assign this event to the $\text{Co}^{\text{II}}_2/\text{Co}^{\text{I}}\text{Co}^{\text{III}}$ oxidation, which verifies that **1** is inert towards reaction with oxygen in solution.³¹

In order to further assess the stability of **1** under physiological conditions, 10 mM aqueous solutions of the Co_2 complex buffered at pH 7.3 were incubated with 10 mM solutions of the ions $\text{H}_2\text{PO}_4^-/\text{HPO}_4^{2-}$, CO_3^{2-} , SO_4^{2-} , CH_3COO^- , and Ca^{2+} for 16 h at 25 $^{\circ}\text{C}$. The ^1H NMR spectra of these solutions collected at 37 $^{\circ}\text{C}$ appear identical to the spectrum obtained previously at the same pH, albeit showing the additional ions (see Figures S57 and S58). Furthermore, compound **1** exhibits analogous NMR and CEST properties in fetal bovine serum (FBS) as in HEPES buffer in the pH range 6.6–7.6 (see Figures S59–S62). The observation of a slightly broader H_2O resonance in FBS compared to buffer is presumably due to contributions from labile protons of proteins in the serum. Importantly, the highly-shifted CEST peaks for **1** are unaffected by this broadness near the diamagnetic region, and the pH calibration curves obtained in FBS and buffer are essentially identical (see Figure S63). It is important to note that the additional feature at ca. 88 ppm in the CEST spectra does not impact the CEST analysis of **1**. The exact nature of this feature is currently unknown but likely stems from a miniscule amount of an OH-containing impurity, as it is most prominent at acidic pH and no signals are observed in this regime in the corresponding ^1H NMR spectra. Taken together, these results demonstrate the high stability of **1** in physiological environments and suggest its potential for *in vivo* studies.

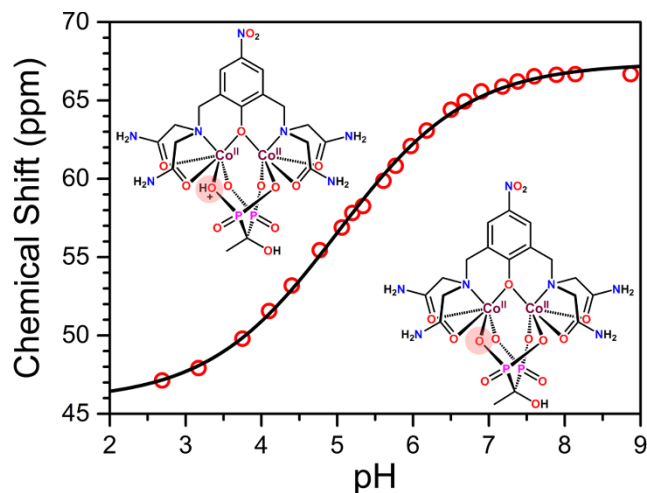


Figure 5. ^1H NMR chemical shift (frequency offset) of the CH_3 resonance from etidronate vs pH for aqueous buffer solutions of **1**. Red circles denote experimental data, and the black line corresponds to a sigmoidal fit of the data (Equation 1). Inset: Schematics of the anion from **1**, highlighting the protonation state of etidronate.

To further investigate the biocompatibility of **1**, preliminary cell viability experiments were carried out using melanoma B16F10 cells as a model. The study revealed that >50% of the cells are viable after incubation with millimolar concentrations of **1** for 24 h (see Figure S64). Note that the %viability values are reported without taking normal cell death into account, which can be appreciable, and thus only correspond to the lower limits of cell survivals at given probe concentrations (see Experimental Section).

NMR Studies of pH-Induced Structural Changes. In addition to changes in CEST peak intensities with pH, variations in the frequency of CEST peaks may also be employed for ratiometric pH sensing.^{7ac} Such CEST frequency changes are typically caused by a pH-dependent interconversion between species of different protonation states.⁷ Indeed, the CEST peaks for **1–3** show slight shifts with pH, which suggests modest structural changes in solution. To gain further insight into potential pH-induced structural changes in the Co_2 complexes, ^1H NMR spectra were collected for samples of **1–3** in aqueous buffer solutions over a broad pH range. The carboxamide peaks for **1** show moderate changes in chemical shifts between pH 2.69 and 8.87 (see Figure S65), while the CH_3 resonance from etidronate shifts dramatically, by 19.55 ppm, following a sigmoidal pH profile.

A fit of the CH_3 chemical shift vs pH data to Equation 1 gave a pK_a value of 5.01(3) (see Figure 5). Similarly, the etidronate CH_3 resonance for **3** shifts from 44.00 to 62.68 ppm in the pH range 1.56–8.82, and a corresponding sigmoidal fit of the data afforded a value of $\text{pK}_a = 5.28(5)$ (see Figure S66). In addition, the changes in resonance frequencies of the carboxamides for **2** resemble those for **1**, albeit less pronounced (see Figure S67). Comparably, a fit of the chemical shift vs pH data for the CH resonance from CMDP^{4-} to Equation 1 yielded a pK_a of 4.40(2) (see Figure S68). These dramatic pH-dependent chemical shift changes of the CH_3 and CH resonances from the bisphosphonates strongly suggest that the ancillary ligands become protonated at low pH. The similar trends observed for all complexes and the excellent agreement of the data to a model for a single ionization event, together with the pK_a values of the free bisphosphonic acids,³² are most

consistent with protonation/deprotonation of one of the cobalt-coordinated P–O oxygen atoms as the source of peak shifts in this pH range (see Figure 5, inset). Indeed, protonated phosphate oxygen donors have been observed in the solid-state in transition metal bisphosphonate complexes.³³

The observation of a considerably lower pK_a for **2** than **1** is in accord with the insignificant variation in CEST frequencies of the amide peaks for **2**, as CMDP^{4-} is nearly completely deprotonated above pH 6.5. Furthermore, the value of $pK_a = 5.28(5)$ for **3** is in line with the observed pH dependence of the hydroxyl CEST frequency. This behavior stems from transitioning from a state with considerable contributions from both protonation states of etidronate at pH 5.8, to a state with near exclusively the fully deprotonated ligand above pH 7.1. Finally, these NMR studies establish the integrity of **1–3** in aqueous solutions over a wide pH range.

MR Phantom Imaging. To further examine the practicality of **1** for ratiometric pH imaging through PARACEST, CEST images of phantoms containing a series of 17 mM aqueous solutions of **1** buffered at selected pH values from 6.40 to 7.88 were collected on a 17.6 T MRI scanner. For each pH value, two images were acquired at 37 °C after irradiation at 64 and 104 ppm vs H_2O , respectively, using 74.3 μT presaturation pulses. Corresponding control images were collected at 0 ppm frequency offset with 0 μT power. Note that the high

presaturation power was required to saturate the labile protons of **1** owing to the larger Zeeman splitting on the 17.6 T MRI scanner. The %CEST at 64 ppm increased from 1.1 to 24% upon moving from pH 6.40 to 7.88, while presaturation at 104 ppm afforded values of 5.4 to 15% within this range (see Figures S69 and 6, upper). These pH-dependent trends in CEST intensity are consistent with those observed in the NMR study. Moreover, the ratio of CEST intensities at 104 and 64 ppm ($\text{CEST}_{104 \text{ ppm}}/\text{CEST}_{64 \text{ ppm}}$) decreased substantially from pH 6.58 to 7.54 (see Figures S70 and 6, lower left), and a plot of log of the ratios between averaged phantom intensities at these frequencies ($\log(\text{CEST}_{104 \text{ ppm}}/\text{CEST}_{64 \text{ ppm}})$) vs pH gave an excellent linear fit in analogy to Equations 3–9 (see Figure S70, inset). Using this calibration curve and the $\text{CEST}_{104 \text{ ppm}}/\text{CEST}_{64 \text{ ppm}}$ values per pixel, a pH map was generated (see Figure 6, lower right). This result highlights that the pH-dependent changes in CEST intensity ratios can be clearly visualized by MRI. Furthermore, the pH values calculated from the calibration curve are in good agreement with those independently measured by a pH electrode (see Table S7). In sum, phantom imaging experiments further demonstrate the ability of **1** to ratiometrically quantitate solution pH in the physiological pH range 6.5–7.6. Future efforts will be geared toward improving the homogeneity and overall quality of CEST images through pulse sequence optimization, as well as to investigate the feasibility of pH imaging with **1** on lower

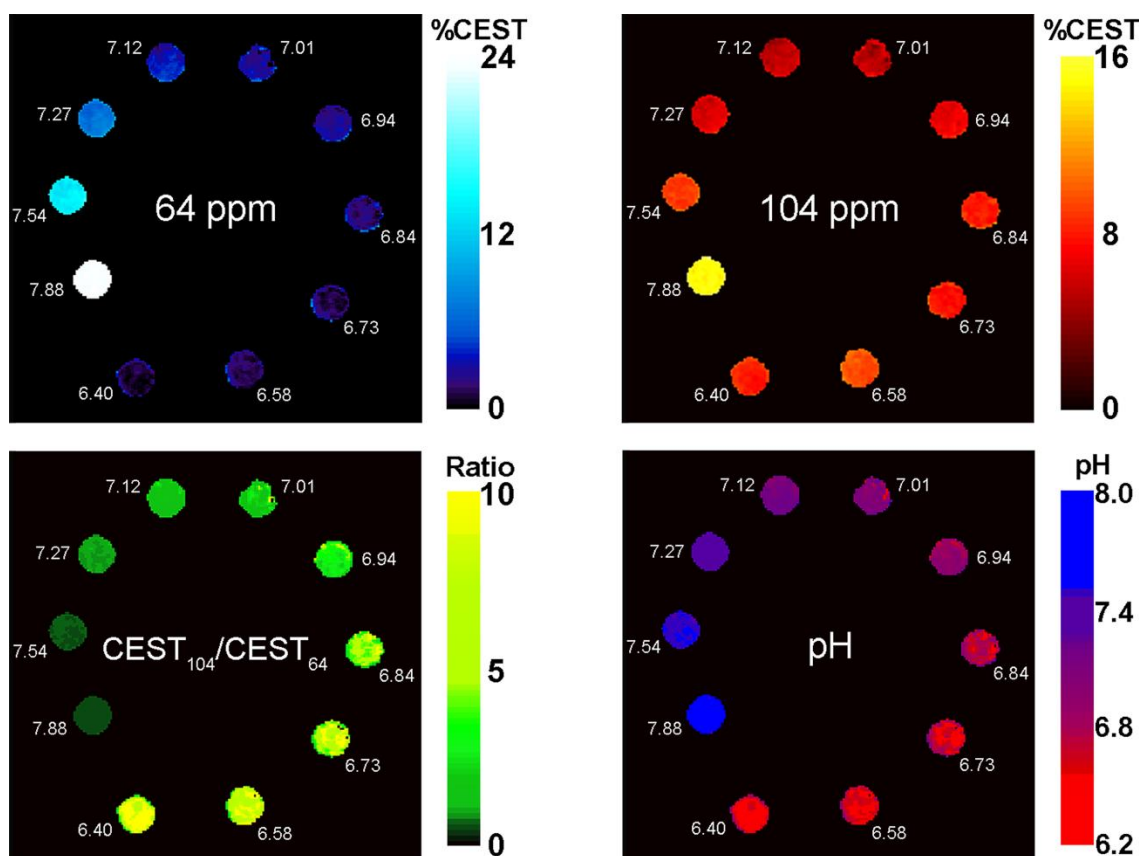


Figure 6. CEST images of phantoms containing 17 mM aqueous buffer solutions of **1** in the pH range 6.40–7.88, collected at 37 °C on a 17.6 T MRI scanner. Upper: Images constructed from CEST effect upon presaturation at 64 ppm (left) and 104 ppm (right), respectively. Lower: Ratiometric $\text{CEST}_{104 \text{ ppm}}/\text{CEST}_{64 \text{ ppm}}$ map obtained by taking the pixel-wise ratios of CEST signal intensities at 104 and 64 ppm (left), and a pixel-wise pH map calculated from the corresponding $\log(\text{CEST}_{104 \text{ ppm}}/\text{CEST}_{64 \text{ ppm}})$ values by using the calibration curve displayed in Figure S70, obtained from averaged phantom intensities at 64 and 104 ppm between pH 6.58 and 7.54 (right). White numbers next to each phantom sample denote the pH of the corresponding solution measured by a pH electrode.

field MRI scanners. Eventually, the actual potential of the Co^{II} probe for ratiometric mapping of pH will be evaluated in small animal imaging studies.

CONCLUSIONS AND OUTLOOK

The foregoing results demonstrate the ability of Co_2 complexes to provide a concentration-independent measure of solution pH over a range relevant for detecting physiological abnormalities through ratiometric PARACEST imaging. In particular, the systematic study of 1–3 illustrates the opposing pH-dependent CEST properties of carboxamide NH and etidronate OH protons. The potential of Co^{II} complexes as ratiometric pH probes is further highlighted by the stability of 1 in physiological environments and good agreement between pH from phantom images of 1 and those measured by an electrode. Considering the excellent tunability of the phenoxo-bridged dinuclear platform, ongoing work is focused on investigating the CEST behavior of related ancillary bisphosphonate ligands, and on incorporating other CEST-active functional groups on the dinucleating ligand scaffold, in efforts to optimize the pH-dependent CEST properties of this family of molecules for imaging pH *in vivo*. We anticipate that this broadly generalizable platform will aid in developing pH-responsive probes with higher sensitivity and stability, in particular those suitable for *in vivo* applications.

ASSOCIATED CONTENT

Supporting Information

Additional experimental details and characterization data for 1, 2, and 3, including crystallographic data for 1' and 2'. This material is available free of charge via the Internet at <http://pubs.acs.org>.

AUTHOR INFORMATION

Corresponding Author

*dharris@northwestern.edu

ORCID

Agnes E. Thorarinsdottir: 0000-0001-9378-4454

Kang Du: 0000-0001-9947-2320

T. David Harris: 0000-0003-4144-900X

Notes

The authors declare no competing financial interests.

ACKNOWLEDGMENT

This research was funded by the Air Force Research Laboratory under agreement no. FA8650-15-5518 and Northwestern University. T.D.H. thanks the Alfred P. Sloan Foundation, and A.E.T. gratefully acknowledges the Leifur Eiriksson Foundation for funding support. X-ray crystallography and NMR spectroscopy was performed at the Integrated Molecular Structure Education and Research Center (IMSERC) at Northwestern University, with support from the Soft and Hybrid Nanotechnology Experimental (SHyNE) Resource (NSF NNCI-1542205), the State of Illinois, and International Institute for Nanotechnology (IIN). Quantitative analysis of Co and P was performed at the Northwestern University Quantitative Bio-element Imaging Center. We thank Prof. T. J. Meade for generous donation of B16F10 cell supplies, fetal bovine serum, and for use of his HPLC system, lyophilizer, and laminar flow hood, Prof. C. A. Mirkin for use of his flow cytometer, Dr. L. M. Lilley for experimental assistance and

helpful discussions, and Mr. G. Yamankurt and Mr. S. M. Tatro for experimental assistance.

REFERENCES

- (1) (a) Kallinowski, F.; Schlenger, K. H.; Runkel, S.; Kloes, M.; Stohrer, M.; Okunieff, P.; Vaupel, P. *Cancer Res.* **1989**, *49*, 3759. (b) Tannock, I. F.; Rotin, D. *Cancer Res.* **1989**, *49*, 4373. (c) Vaupel, P.; Kallinowski, F.; Okunieff, P. *Cancer Res.* **1989**, *49*, 6449. (d) Gillies, R. J.; Raghunand, N.; Karczmar, G. S.; Bhujwala, Z. M. *J. Magn. Reson. Imaging* **2002**, *16*, 430. (e) Gatenby, R. A.; Gillies, R. J. *Nat. Rev. Cancer* **2004**, *4*, 891. (f) Gillies, R. J.; Raghunand, N.; Garcia-Martin, M. L.; Gatenby, R. A. *IEEE Eng. Med. Biol. Mag.* **2004**, *23*, 57. (g) Hashim, A. I.; Zhang, X.; Wojtkowiak, J. W.; Martinez, G. V.; Gillies, R. J. *NMR Biomed.* **2011**, *24*, 582. (h) Kato, Y.; Ozawa, S.; Miyamoto, C.; Maehata, Y.; Suzuki, A.; Maeda, T.; Baba, Y. *Cancer Cell Int.* **2013**, *13*, 89.
- (2) (a) Katsura, K.; Ekholm, A.; Asplund, B.; Siesjö, B. K. *J. Cereb. Blood Flow Metab.* **1991**, *11*, 597. (b) Sun, P. Z.; Wang, E.; Cheung, J. S. *Neuroimage* **2012**, *60*, 1. (c) Rajamäki, K.; Nordström, T.; Nurmi, K.; Åkerman, K. E. O.; Kovanen, P. T.; Öörni, K.; Eklund, K. K. *J. Biol. Chem.* **2013**, *288*, 13410.
- (3) (a) Wike-Hooley, J. L.; Haveman, J.; Reinhold, H. S. *Radiother. Oncol.* **1984**, *2*, 343. (b) Gerweck, L. E.; Seetharaman, K. *Cancer Res.* **1996**, *56*, 1194. (c) Wojtkowiak, J. W.; Verduzco, D.; Schramm, K. J.; Gillies, R. J. *Mol. Pharm.* **2011**, *8*, 2032. (d) Pilon-Thomas, S.; Kodumudi, K. N.; El-Kenawi, A. E.; Russell, S.; Weber, A. M.; Luddy, K.; Damaghi, M.; Wojtkowiak, J. W.; Mulé, J. J.; Ibrahim-Hashim, A.; Gillies, R. J. *Cancer Res.* **2016**, *76*, 1381.
- (4) (a) Lauffer, R. B. *Chem. Rev.* **1987**, *87*, 901. (b) Caravan, P.; Ellison, J. J.; McMurry, T. J.; Lauffer, R. B. *Chem. Rev.* **1999**, *99*, 2293. (c) Rieke, V.; Pauly, K. B. *J. Magn. Reson. Imaging* **2008**, *27*, 376.
- (5) Ward, K. M.; Aletras, A. H.; Balaban, R. S. *J. Magn. Reson.* **2000**, *143*, 79.
- (6) Selected references: (a) Zhang, S.; Winter, P.; Wu, K.; Sherry, A. D. *J. Am. Chem. Soc.* **2001**, *123*, 1517. (b) Zhang, S.; Merritt, M.; Woessner, D. E.; Lenkinski, R. E.; Sherry, A. D. *Acc. Chem. Res.* **2003**, *36*, 783. (c) Zhou, J.; van Zijl, P. C. M. *Prog. Nucl. Magn. Reson. Spectrosc.* **2006**, *48*, 109. (d) Woods, M.; Woessner, D. E.; Sherry, A. D. *Chem. Soc. Rev.* **2006**, *35*, 500. (e) Ali, M. M.; Liu, G.; Shah, T.; Flask, C. A.; Pagel, M. D. *Acc. Chem. Res.* **2009**, *42*, 915. (f) Viswanathan, S.; Kovacs, Z.; Green, K. N.; Ratnakar, S. J.; Sherry, A. D. *Chem. Rev.* **2010**, *110*, 2960. (g) Terreno, E.; Castelli, D. D.; Viale, A.; Aime, S. *Chem. Rev.* **2010**, *110*, 3019. (h) Soesbe, T. C.; Wu, Y.; Sherry, A. D. *NMR Biomed.* **2013**, *26*, 829.
- (7) (a) Wu, Y.; Soesbe, T. C.; Kiefer, G. E.; Zhao, P.; Sherry, A. D. *J. Am. Chem. Soc.* **2010**, *132*, 14002. (b) Wang, X.; Wu, Y.; Soesbe, T. C.; Yu, J.; Zhao, P.; Kiefer, G. E.; Sherry, A. D. *Angew. Chem., Int. Ed.* **2015**, *54*, 8662. (c) Wu, Y.; Zhang, S.; Soesbe, T. C.; Yu, J.; Vinogradov, E.; Lenkinski, R. E.; Sherry, A. D. *Magn. Reson. Med.* **2016**, *75*, 2432. (d) Tsitovich, P. B.; Cox, J. M.; Sperry, J. A.; Morrow, J. R. *Inorg. Chem.* **2016**, *55*, 12001.
- (8) McVicar, N.; Li, A. X.; Suchý, M.; Hudson, R. H. E.; Menon, R. S.; Bartha, R. *Magn. Reson. Med.* **2013**, *70*, 1016.

- (9) (a) Aime, S.; Castelli, D. D.; Terreno, E. *Angew. Chem., Int. Ed.* **2002**, *41*, 4334. (b) Castelli, D. D.; Terreno, E.; Aime, S. *Angew. Chem., Int. Ed.* **2011**, *50*, 1798. (c) Liu, G.; Li, Y.; Sheth, V. R.; Pagel, M. D. *Mol. Imaging* **2012**, *11*, 47. (d) Sheth, V. R.; Liu, G.; Li, Y.; Pagel, M. D. *Contrast Media Mol. Imaging* **2012**, *7*, 26. (e) Sheth, V. R.; Li, Y.; Chen, L. Q.; Howison, C. M.; Flask, C. A.; Pagel, M. D. *Magn. Reson. Med.* **2012**, *67*, 760. (f) Dorazio, S. J.; Olatunde, A. O.; Sperryak, J. A.; Morrow, J. R. *Chem. Commun.* **2013**, *49*, 10025. (g) Castelli, D. D.; Ferrauto, G.; Cutrin, J. C.; Terreno, E.; Aime, S. *Magn. Reson. Med.* **2014**, *71*, 326. (h) Rancan, G.; Castelli, D. D.; Aime, S. *Magn. Reson. Med.* **2016**, *75*, 329. (i) Krchová, T.; Gálisová, A.; Jiráček, D.; Hermann, P.; Kotek, J. *Dalton Trans.* **2016**, *45*, 3486.
- (10) (a) Wolff, S. D.; Balaban, R. S. *Magn. Reson. Med.* **1989**, *10*, 135. (b) Zaiss, M.; Bachert, P. *Phys. Med. Biol.* **2013**, *58*, R221.
- (11) Selected references: (a) Dorazio, S. J.; Tsitovich, P. B.; Sitters, K. E.; Sperryak, J. A.; Morrow, J. R. *J. Am. Chem. Soc.* **2011**, *133*, 14154. (b) Dorazio, S. J.; Morrow, J. R. *Eur. J. Inorg. Chem.* **2012**, 2006. (c) Dorazio, S. J.; Tsitovich, P. B.; Gardina, S. A.; Morrow, J. R. *J. Inorg. Biochem.* **2012**, *117*, 212. (d) Tsitovich, P. B.; Morrow, J. R. *Inorg. Chim. Acta* **2012**, *393*, 3. (e) Olatunde, A. O.; Dorazio, S. J.; Sperryak, J. A.; Morrow, J. R. *J. Am. Chem. Soc.* **2012**, *134*, 18503. (f) Dorazio, S. J.; Morrow, J. R. *Inorg. Chem.* **2012**, *51*, 7448. (g) Tsitovich, P. B.; Sperryak, J. A.; Morrow, J. R. *Angew. Chem., Int. Ed.* **2013**, *52*, 13997. (h) Dorazio, S. J.; Olatunde, A. O.; Tsitovich, P. B.; Morrow, J. R. *J. Biol. Inorg. Chem.* **2014**, *19*, 191. (i) Jeon, I.-R.; Park, J. G.; Haney, C. R.; Harris, T. D. *Chem. Sci.* **2014**, *5*, 2461. (j) Olatunde, A. O.; Bond, C. J.; Dorazio, S. J.; Cox, J. M.; Benedict, J. B.; Daddario, M. D.; Sperryak, J. A.; Morrow, J. R. *Chem. Eur. J.* **2015**, *21*, 18290. (k) Tsitovich, P. B.; Cox, J. M.; Benedict, J. B.; Morrow, J. R. *Inorg. Chem.* **2016**, *55*, 700. (l) Du, K.; Harris, T. D. *J. Am. Chem. Soc.* **2016**, *138*, 7804. (m) Du, K.; Waters, E. A.; Harris, T. D. *Chem. Sci.* **2017**, *8*, 4424. (n) Burns, P. J.; Cox, J. M.; Morrow, J. R. *Inorg. Chem.* **2017**, *56*, 4545.
- (12) (a) James, T. L. *Nuclear Magnetic Resonance in Biochemistry: Principles and Applications*; Academic Press: New York, 1975. (b) Bertini, I.; Luchinat, C. *NMR of Paramagnetic Molecules in Biological Systems*; The Benjamin/Cummings Publishing Company, Inc.: Menlo Park, 1986. (c) Bertini, I.; Luchinat, C. *Coord. Chem. Rev.* **1996**, *150*, 1. (d) Bertini, I.; Luchinat, C.; Parigi, G. *Solution NMR of Paramagnetic Molecules: Applications to Metallobiomolecules and Models*; Elsevier Science B.V.: Amsterdam, 2001.
- (13) APEX2, version 2014.11-0; Bruker Analytical X-ray Systems, Inc.: Madison, WI, 2014.
- (14) Sheldrick, G. M. *SADABS*, version 2.03; Bruker Analytical X-ray Systems, Inc.: Madison, WI, 2000.
- (15) (a) Sheldrick, G. M. *SHELXTL*, version 6.12; Bruker Analytical X-ray Systems, Inc.: Madison, WI, 2000. (b) Sheldrick, G. M. *Acta Crystallogr., Sect. A: Found. Adv.* **2015**, *71*, 3.
- (16) Dolomanov, O. V.; Bourhis, L. J.; Gildea, R. J.; Howard, J. A. K.; Puschmann, H. *J. Appl. Crystallogr.* **2009**, *42*, 339.
- (17) *OriginPro*, version 9.0; OriginLab, Corp.: Northampton, MA, 2003.
- (18) Dixon, W. T.; Ren, J.; Lubag, A. J. M.; Ratnakar, J.; Vinogradov, E.; Hancu, I.; Lenkinski, R. E.; Sherry, A. D. *Magn. Reson. Med.* **2010**, *63*, 625.
- (19) (a) Chen, L. Q.; Howison, C. M.; Jeffery, J. J.; Robey, I. F.; Kuo, P. H.; Pagel, M. D. *Magn. Reson. Med.* **2014**, *72*, 1408. (b) Moon, B. F.; Jones, K. M.; Chen, L. Q.; Liu, P.; Randtke, E. A.; Howison, C. M.; Pagel, M. D. *Contrast Media Mol. Imaging* **2015**, *10*, 446.
- (20) Aime, S.; Barge, A.; Castelli, D. D.; Fedeli, F.; Mortillaro, A.; Nielsen, F. U.; Terreno, E. *Magn. Reson. Med.* **2002**, *47*, 639.
- (21) (a) Evans, D. F. *J. Chem. Soc.* **1959**, 2003. (b) Schubert, E. M. *J. Chem. Educ.* **1992**, *69*, 62.
- (22) Bain, G. A.; Berry, J. F. *J. Chem. Educ.* **2008**, *85*, 532.
- (23) Sawyer, D. T.; Sobkowiak, A. J.; Roberts, J. *Electrochemistry for Chemists*, 2nd ed.; John Wiley & Sons: New York, 1995.
- (24) Selected references: (a) Sakiyama, H.; Ito, R.; Kumagai, H.; Inoue, K.; Sakamoto, M.; Nishida, Y.; Yamasaki, M. *Eur. J. Inorg. Chem.* **2001**, 2027. (b) Hossain, M. J.; Yamasaki, M.; Mikuriya, M.; Kuribayashi, A.; Sakiyama, H. *Inorg. Chem.* **2002**, *41*, 4058. (c) Tian, J.-L.; Gu, W.; Yan, S.-P.; Liao, D.-Z.; Jiang, Z.-H. *Z. Anorg. Allg. Chem.* **2008**, *634*, 1775. (d) Daumann, L. J.; Comba, P.; Larrabee, J. A.; Schenk, G.; Stranger, R.; Cavigliasso, G.; Gahan, L. R. *Inorg. Chem.* **2013**, *52*, 2029.
- (25) (a) Johansson, F. B.; Bond, A. D.; Nielsen, U. G.; Mobaraki, B.; Murray, K. S.; Berry, K. J.; Larrabee, J. A.; McKenzie, C. J. *Inorg. Chem.* **2008**, *47*, 5079. (b) Seidler-Egdal, R. K.; Johansson, F. B.; Veltzé, S.; Skou, E. M.; Bond, A. D.; McKenzie, C. J. *Dalton Trans.* **2011**, *40*, 3336.
- (26) (a) Wayland, B. B.; Drago, R. S.; Henneke, H. F. *J. Am. Chem. Soc.* **1966**, *88*, 2455. (b) Stewart, W. E.; Siddall, T. H. *Chem. Rev.* **1970**, *70*, 517. (c) Ming, L.-J.; Lauffer, R. B.; Que, Jr., L. *Inorg. Chem.* **1990**, *29*, 3060.
- (27) Huang, C.-H.; Morrow, J. R. *Inorg. Chem.* **2009**, *48*, 7237.
- (28) (a) Woods, M.; Woessner, D. E.; Zhao, P.; Pasha, A.; Yang, M.-Y.; Huang, C.-H.; Vasality, O.; Morrow, J. R.; Sherry, A. D. *J. Am. Chem. Soc.* **2006**, *128*, 10155. (b) Huang, C.-H.; Morrow, J. R. *J. Am. Chem. Soc.* **2009**, *131*, 4206. (c) Huang, C.-H.; Hammell, J.; Ratnakar, S. J.; Sherry, A. D.; Morrow, J. R. *Inorg. Chem.* **2010**, *49*, 5963. (d) Hammell, J.; Buttarazzi, L.; Huang, C.-H.; Morrow, J. R. *Inorg. Chem.* **2011**, *50*, 4857. (e) Ferrauto, G.; Castelli, D. D.; Terreno, E.; Aime, S. *Magn. Reson. Med.* **2013**, *69*, 1703.
- (29) Note that the common logarithm with base 10 was used throughout this study. For brevity, the notation “log” is employed in the pH calibration equations rather than the precise notation “log₁₀.”
- (30) (a) Ward, K. M.; Balaban, R. S. *Magn. Reson. Med.* **2000**, *44*, 799. (b) Terreno, E.; Castelli, D. D.; Cravotto, G.; Milone, L.; Aime, S. *Invest. Radiol.* **2004**, *39*, 235.
- (31) Wood, P. M. *Biochem. J.* **1988**, *253*, 287.
- (32) (a) Raymond, G. G.; Born, J. L. *Drug Intell. Clin. Pharm.* **1986**, *20*, 683. (b) Vepsäläinen, J. J. *Curr. Med. Chem.* **2002**, *9*, 1201. (c) Alanne, A.-L.; Hyvönen, H.; Lahtinen, M.; Ylisirniö, M.; Turhanen, P.; Kolehmainen, E.; Peräniemi, S.; Vepsäläinen, J. J. *Molecules* **2012**, *17*, 10928.
- (33) (a) Hu, J.; Zhao, J.; Hou, H.; Fan, Y. *Inorg. Chem. Commun.* **2008**, *11*, 1110. (b) Guo, Z.-F.; Li, B.; Guo, J.-Z.; Yang, P.; Shi, L.-F.; Liu, L. *Transition Met. Chem.* **2014**, *39*, 353.

1
2
3
4
5
6
7
8
9
10
11
12
13
14
15
16
17
18
19
20
21
22
23
24
25
26
27
28
29
30
31
32
33
34
35
36
37
38
39
40
41
42
43
44
45
46
47
48
49
50
51
52
53
54
55
56
57
58
59
60

